IEEE Access
Multidisciplinary | Rapid Review | Open Access Journal

Received February 3, 2020, accepted February 21, 2020, date of publication March 4, 2020, date of current version March 19, 2020.

Digital Object Identifier 10.1109/ACCESS.2020.2978248

Permanent Magnet Motor Design for Satellite Attitude Control With High Torque Density and Low Torque Ripple

PO-HUAN CHOU[1], SHIH-CHIN YANG[2], (Senior Member, IEEE), CIAO-JHEN JHONG[2], JEN-I HUANG[2], AND JYUN-YOU CHEN[2], (Student Member, IEEE)

[1]Industrial Technology Research Institute, Hsinchu 31057, Taiwan
[2]Department of Mechanical Engineering, National Taiwan University, Taipei 10617, Taiwan

Corresponding author: Shih-Chin Yang (scy99@ ntu.edu.tw)

This work was supported in part by the Mechanical and Mechatronics Systems Laboratory of Industrial Technology Research Institute under Grant K353C71100, and in part by the Taiwanese Ministry of Science and Technology under Grant 108-2623-E-002-004-D.

ABSTRACT This paper proposes a high-precision permanent magnet (PM) motor primarily used for the satellite attitude control. Considering aerospace applications, the dynamic response, weight and torque ripple are primarily concerns. To achieve the fast response and low ripple, a stator with slotless windings is designed to achieve the ripple free torque production. However, slotless windings contain visible leakage fluxes which might decrease the torque production. In this paper, several design methods are proposed to decrease leakage fluxes by concentrating the flux linkage under slotless topology. First, leakage fluxes caused by slotless windings are minimized through the radial-flux dual-rotor topology. This topology results in the flux linkage concentration in the air gap because two rotors are used separately for flux transmitter and receiver. It is concluded that the dual-rotor is well suited for a slotless windings motor to maximize the air gap flux linkage. Second, Halbach array magnets are chosen to realize the sinusoidal flux linkage distribution. Different array angles are analyzed to minimize the torque ripple. It is shown that the 22.5deg array angle results in the lowest torque ripple among three different Halbach magnets. More importantly, the average torque output is higher comparing to conventional radial magnet magnetization. Although several optimization methods have been developed on the motor geometric design, very few researches focus on the design of dual-rotor slotless windings and air gap length. This design approach further decreases leakage fluxes. In this paper, finite element analysis (FEA) is used for the satellite motor design. In addition, a motor prototype is built for experimental tests.

INDEX TERMS Satellite control, reaction wheel and radial flux motor.

I. INTRODUCTION

Reaction wheel which is the key component for the satellite attitude control system [1], [2]. On this basis, satellite controller includes a flywheel and a motor [3]. By regulating the flywheel angular momentum, the satellite location can be maintained in the space under the influence of disturbance torques [4], [5]. The satellite control is a multidisciplinary topic including the precision motor design [6], 3-dimension attitude control [7] and the safety-critical reliability [8]. This paper aims to design a high-performance PM motor for satellite attitude applications.

The purpose of PM motor include the fast dynamic response, tiny volume, light weight, high efficiency and low torque ripple. Considering the volume reduction, a slotless stator without iron teeth is used to generate stator armature fluxes [9], [10]. In [11], the slotless stator can suppress the armature flux harmonics. Thus, the rotor eddy current losses at high speed is reduced. However, the effective flux density is lower because of the larger equivalent air gap with considerable magnetic flux leakage. This lower flux density disadvantage degrades the torque output comparing to slotted PM motors. Besides in [12], different shapes of slotless

The associate editor coordinating the review of this manuscript and approving it for publication was Gaolin Wang.

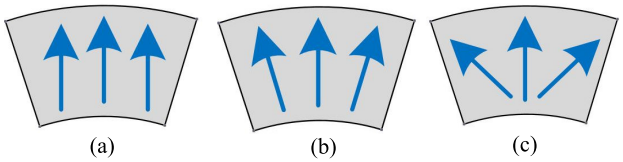

FIGURE 1. Different magnet magnetizations: (a) parallel, (b) radial and (c) sinusoidal distribution.

windings are compared among the armature harmonic, eddy current loss, and current density. The rhombic typed windings result in secondary harmonics on radial armature flux which might increase the torque ripple. In [13], the stator core loss is analyzed for slotless windings under different lamination thicknesses. Because of the skin effect, a thinner lamination is suggested even using slotless windings. These drawbacks related to low torque density, leakage flux and eddy current loss limit slotless windings for satellite applications under the size limitation.

Due to the progress on the magnet fabrication, several magnet magnetization patterns are developed at this time. As seen in Fig. 1, the magnet magnetiziation consists of (a) parallel, (b) radial, and (c) sinusoidal distribution. It is noted that only the fundmental magnet flux harmonic is useful for the torque production. Under this effect, the sinusoidal magnetization is preffered for the torque production at low ripple. In general, the sinusoidal magnetization can be implemented based on mutiple discrete magnets with different magnetization directions, e.g. Halbach array [14]–[16]. Instead of low torque ripples and low flux harmonics, Halbach magnet has the advantage to improve leakage fluxes caused by the slotless stator [15]. In [17]–[19], back electromotive force (EMF) waveforms are compared under different Halbach magnet shapes and Halbach array angles. It is observed that the Halbach array angle is the key to realize a sinusoidal EMF waveform. Besides in [20], magnets with both parallel magnetization and Halbach array are compared based on the torque output capability. For high-pole motors, Halbach magnets can achieve the higher average torque; however for low-pole motors, parallel magnetization magnets are suggested. In addition for bearing motors, Halbach magnets also provide the sufficient radial force to suspen the rotating component [21]. It should be also noted that the fabrication of Halbach magnets is a challenge for fractional slot windings with high pole numbers.

Radial-flux PM motors are designed with dual-stator [22], [23] or dual-rotor [24]–[26] for the torque improvement. For the design of dual-stator, two separated inverters can be applied to two stators separately. This design increases the power density using two segment PWM inverters to decrease the power loading [22]. Unfortunately, dual-stator with the complicated topology might not be useful for satellite applications. By contrast, the dual-rotor topology is simpler with only one stator between two rotors [25]. Besides in [24], a dual-rotor motor is developed with two independent rotating speed simultaneously for air condition applications. In [26],

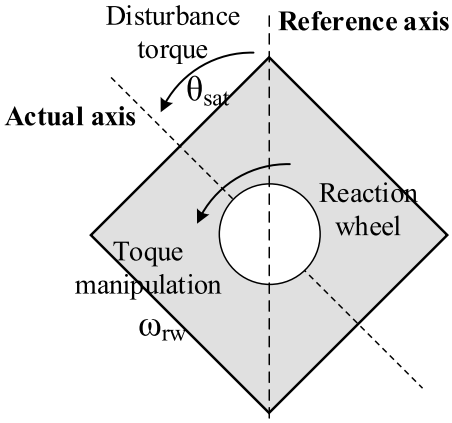

FIGURE 2. Satellite attitude control under the external disturbance.

multiple rotors and slotless stators are combined to increase the torque density on a low power motor. In [27], the dual rotors are used respectively for the flux transimmer and receiver to concentrate the flux linkage for the stator with slotless windings.

This paper proposes a satellite motor to improve the torque density through slotless windings and Halbach magnets. The proposed motor design is extended from [27] with comprehensive analysis on the slotlless windings and Halbach magents. In general, slotless windings contain visible leakage fluxes which might decrease the torque production. Several motor design methods are developed to minimize leakage fluxes caused by slotless windings. First, the torque density of slotless PM motor is increased based on the proposed dual-rotor. By designing dual-rotor Halbach array, the overall flux density distribution is concentrated on the air gap for the torque production. Second, Halbach magnets with specific array angles are determined to realize the sinusoidal magnet flux distribution. Comparing to conventional radial or parallel array magnets, Halbach magnets concentrate the flux linkage across air gap. Third, the geometry of dual-rotor is adjusted to minimize the tangential flux in air gap. It is concluded that leakage fluxes can be minimized based on the design of air gap radius and length. In this paper, the two-dimensional electromagnetic flux and torque analysis is confirmed by FEA software package, JMAG Designer. Finally, a motor prototype is fabricated for the experimental verification.

II. SATELLITE OPERATING PRINCIPLE

The principle of satellite control is explained in this section. Fig. 2 shows the satellite control strategy. Considering a small perturbation from the external disturbance T_d, the satellite attitude deviation might appears due to the angular rotation. This disturbance reflected angular momentum H_{sat} is shown to be

$$H_{sat} = J_{sat}\frac{d\theta_{sat}}{dt} \tag{1}$$

where J_{sat} is the satellite inertia and θ_{sat} is the angular position. To maintain the satellite attitude without the

TABLE 1. Satellite motor design objective.

Performance Indices	Values
Weight	500 g
Volume	80×60×40 mm^3
Peak Momentum	0.12 Nm-sec
Normal Momentum	0.06 Nm-sec
Torque output	0.02 Nm
Torque ripple	1% (peak-to-peak)
Rated Speed	6000rpm

self-rotation, another momentum H_{rw} can be generated by rotating the satellite PM motor. It is given by

$$H_{rw} = J_{rw}\left(\omega_{rw} + \frac{d\theta_{sat}}{dt}\right) \tag{2}$$

In (2), J_{rw} and ω_{rw} are respectively the motor inertia and angular speed. Based on the angular momentum conservation, the disturbance T_d can be contributed as

$$T_d = \frac{d\,(H_{sat} + H_{rw})}{dt} \tag{3}$$

At steady state, the corresponding disturbance reflected impulse is shown by

$$\int T_d dt = J_{rw}\,(\omega_{rw} - \omega_o) + (J_{sat} + J_{rw})\,\frac{d\theta_s}{dt} \tag{4}$$

In (4), ω_o is the motor initial angular speed. Considering the satellite attitude control, the angular speed $\omega_{sat} = d\theta_{sat}/dt$ is controlled by zero. As a result, (4) is reorganized by

$$\int T_d dt = J_{rw} \times (\omega_{rw} - \omega_o) = J_{rw}\Delta\omega \tag{5}$$

In (5), $\Delta\omega$ is the motor speed change rate. It is seen that the influence of disturbance T_d is compensated by the motor momentum, change $J_{rw}\Delta\omega$. This momentum change can be used to control the satellite attitude control.

For the purpose to compensate disturbance T_d, a high J_{rw} PM motor is expected, as derived in (5). However, the overall weight and volume of motor should be minimized for satellite applications. With these constraint, satellite motor design objective are listed in Table 1. It is noteworthy that the weight is limited at 500g for the size of micro satellite. The rated speed should be increased to 6000rpm to provide enough H_{rw}. Besides, the torque ripple is limited at 1% peak-to-peak error to achieve the precision reaction wheel control.

III. DUAL-ROTOR DESIGN

This section proposes a topology based on the dual-rotor PM motor. Different slot and rotor topologies, and winding configurations are compared to find a suited satellite motor. Fig. 3 compares three different slotless PM motor topologies. In (a), the inner rotor PM motor is analyzed where the slotless windings are attached on the outer stator iron core. In (b), the outer rotor PM motor is designed where the windings are on the inner stator. Finally, in (c), the dual-rotor PM motor is proposed where the windings are fixed through the polyether ether ketone (PEEK) in the middle of two rotors.

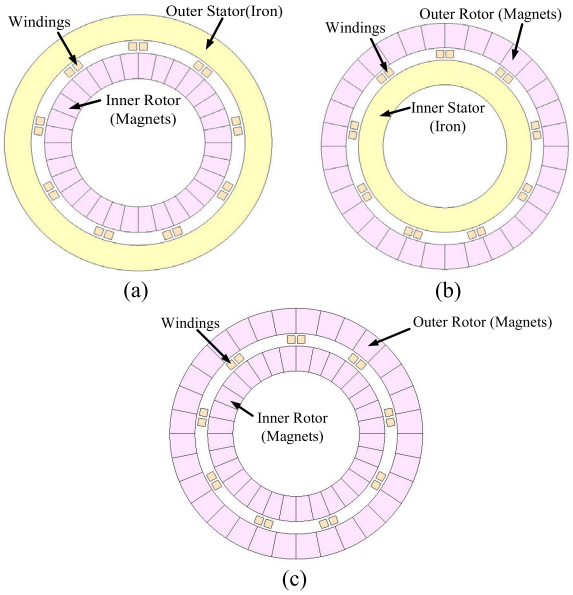

FIGURE 3. Comparison of three motor topologies: (a) single inner rotor, (b) single outer rotor and (c) dual-rotor.

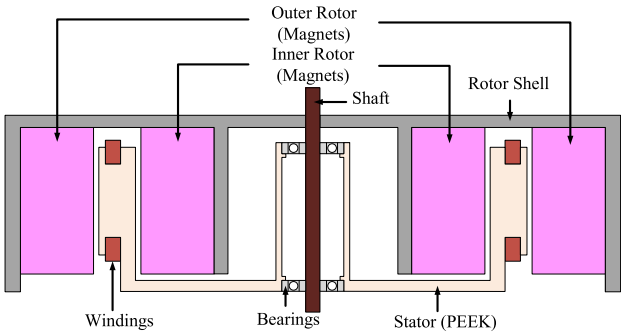

FIGURE 4. The diagram of dual-rotor PM motor assembly.

It is noted that these three motors have the same slot and pole numbers as well as the same rated speed. More importantly, the dual-rotor motor can generate the highest torque output among these three topologies. Thus, the dual-rotor PM motor is chosen for the following design refinement. Fig. 4 shows the diagram of dual-rotor motor assembly. In this topology, both inner and outer rotor of dual-rotor motor are coupled together by a single shaft through a rotor shell. Under this design, the torque can be generated through the single shaft similar to single rotor motor.

Fig. 5 compares different slots and poles combinations for the proposed dual-rotor motor. In this comparison, 8 rotor poles are fixed with respect to different slots. It is noted that for designed slotless motors in this paper, the windings are directly attached on the non-magnetic material, as seen in Fig. 4. Thus, the slotless motor still makes windings in the same slotted area similar to the slotted motor. Under this effect, the slotless windings can be designed with different slot numbers. Fig. 5(a) and (b) demonstrates the winding configuration respectively for 12-slot-8-pole and 9-slot-8-pole motor. First for 12-slot stator in (a), the windings are designed

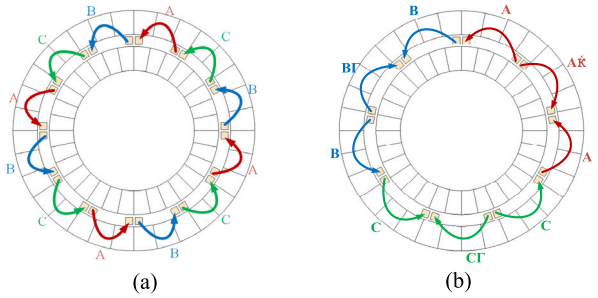

FIGURE 5. Comparison of two different winding contributions: (a) distribution windings (12-slot-8-pole) and (b) concentrated windings (9-slot-8-pole).

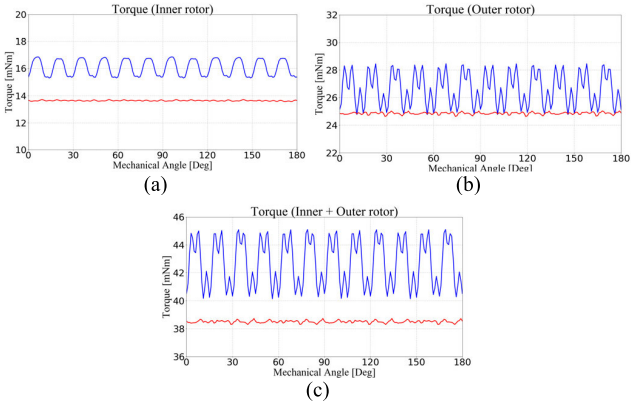

FIGURE 6. Comparison of torque waveform between 12-slot-8-pole and 9-slot-8-pole motors with the topology: (a) inner rotor, (b) outer rotor and (c) dual-rotor.

by *ACBACBACBACB*, where A/B/C are corresponding A-, B- and C-phase windings. By contrast for 9-slot in (b), the windings are *AA'ABB'BCC'C*, where the superscript' represents the inverse windings.

Based on FEA simulation, Fig. 6 evaluates the torque waveform for the motor with 12-slot-8-pole and 9-slot-8-pole. Consiering the FEA setup, the slide mesh is used for the FEA model because of the cylindrical motor shape. Considering the motor size listed in table 1, the element mesh of motor itself is 0.3mm while the air gap region is reduced to 0.1mm. It is noted that the accuracy of FEA results can be improved by further reducing the mesh element size in the air gap region

Fig. 6(a) and (b) compares the torque generated by only inner and outer rotor. As seen from the torque performance comparison in Table 2, the torque ripple is higher on the outer rotor using both 12-slot and 9-slot. However, by selecting 9-slot motor, the torque ripple can be suppressed. For the torque generated by dual-rotor in Fig. 6(c), 9-slot windings achieve a smoother torque waveform though the average torque is lower comparing to 12-slot. As reported in [27], the similar combination of slot and pole, 9-slot-8-pole and 12-slot-10-pole, results in higher winding factors leading to better torque outputs. However, comparing to 8-pole rotor,

TABLE 2. Torque comparison between 12-slot-8-pole motor and 9-slot-8-pole motor in Fig. 5.

Average torque [mNm]	Values
12-slot-8-pole (inner rotor)	16.06
12-slot-8-pole (outer rotor)	26.62
12-slot-8-pole (dual-rotor)	42.69
9-slot-8-pole (inner rotor)	13.64
9-slot-8-pole (outer rotor)	24.86
9-slot-8-pole (dual-rotor)	38.50
Torque ripple [%]	**Values**
12-slot-8-pole (inner rotor)	9.73
12-slot-8-pole (outer rotor)	13.84
12-slot-8-pole (dual-rotor)	11.62
9-slot-8-pole (inner rotor)	1.06
9-slot-8-pole (outer rotor)	1.63
9-slot-8-pole (dual-rotor)	1.13

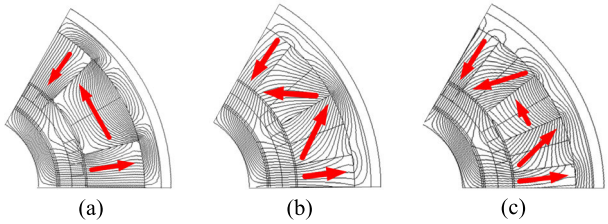

FIGURE 7. Illustration of different Halback magnet segments: (a) n = 2 (90deg), (b) n = 3 (60deg) and (c) n = 4 (45deg).

10-pole might increase the rotor fabrication complexity especially when segment magnet techniques are selected in order to generate the sinusoidal EMF waveform. Considering the manufacturing limitation on high-precision satellite motors, 8-pole rotor and 9-slot windings are combined for the preliminary satellite motor topology.

Because of asymmetric windings for 9-slot-8-pole motor, the unbalanced radial force might occur on the rotor. However, for the proposed motor, a dual-rotor is designed. Comparing to the single-rotor motor topology, unbalanced magnetic force along the radial direction is cancelled even with an odd slot number. Thus, the magnitude of unbalanced force is decreased, leading to the better rotation performance. Besides, the unbalanced force along the tangential direction can be further reduced by modifying the pole numbers, as reported in [28].

IV. HALBACH MAGNET ARRAY

This section explains the EMF and torque performance among different Halbach array magnetizations. As mentioned in [16], Halbach array mangets can increase the average torque and reduce the ripple. This paper focuses on the Halbach magnet design for the dual-rotor slotless stator motor.

In general, the Halbach array is arraged by combining magnets with rotating magnetization direction. Fig. 7 shows three Halbach array magnets where the segment number and array angle are repsectivey (a) n = 2 (90deg), (b) n = 3(60deg) and (c) n = 4 (45deg). Based on FEA simulation, Fig. 8 compares EMF waveforms among different Halbach segment numbers. Considering the ideal condition, the magnet flux distribution is close to the sinusodial waveform by increasing the segment

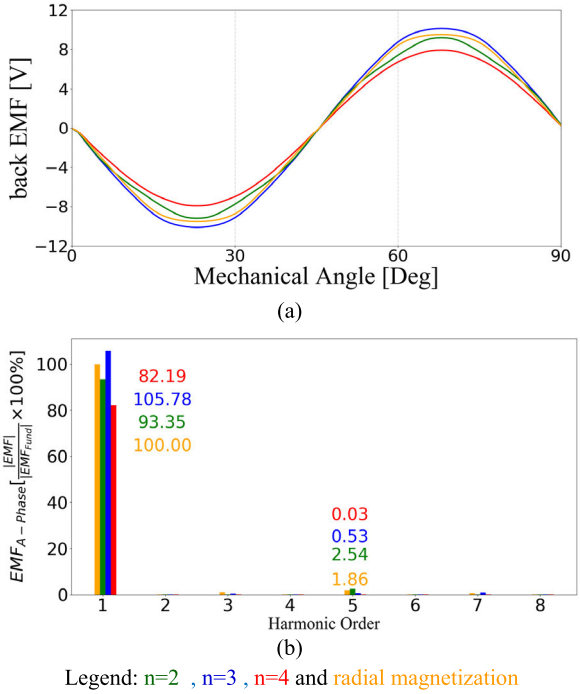

FIGURE 8. EMF waveforms for different magnet magnetizations: Halbach segment n = 2, n = 3, n = 4 and radial magnetization (9-slot-8-pole dual-rotor motor).

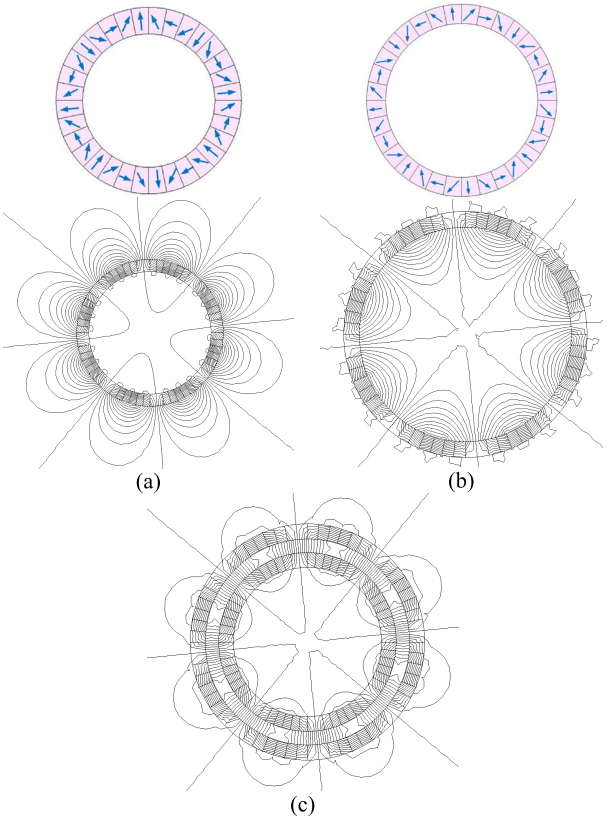

FIGURE 9. Halbach array for the motor with (a) inner rotor, (b) outer rotor and (c) dual-rotor (Segment number n = 4).

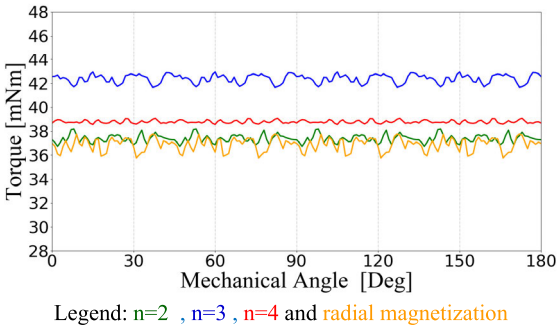

FIGURE 10. Torque waveform with respect to different magnet magnetizations: Halbach segment n = 2, n = 3, n = 4 and radial magnetization (9-slot-8-pole and dual-rotor motor).

number with more array angles. However, it is a challenge to install rotors on small size motors as more Halbach segments used. In this paper, the ferrite material is selected to realize the topology of Halbach magnet array. For the actual prototype fabrication, Halbach magnet segments with different array angles are magnetized firstly. After that, all magnet segments are combined together to implement the Halbach array during the rotor assembly process.

It is important that for the proposed dual-rotor motor, Halbach patterns should be different with respect to the inner rotor and outer rotor to formulate the flux linkage. Fig. 9 compares the magnet flux distribution for (a) inner rotor and (b) outer rotor. In this case, the Halbach array number is n = 4. In general, the magnet flux flows counter-clockwise from north pole to south pole. For the inner rotor, the Halbach array should be arranged by (a) to provide the flux linkage flowing into the outer rotor. By contrast for the outer rotor, the Halbach array is designed by (b) to regulate the flux into the inner rotor. By combining the pattern from both Fig. 9(a) and (b), the Halbach array can be designed by (c).

Fig. 10 shows the torque waveform for the proposed 9-slot-8-pole dual-rotor motor with different magnet magnetizations. In this simulation, Halbach magnets with segment n = 2, 3 and 4, and the radial magnetization magnet in Fig. 1(b) are evaluated. By comparing different magnet magnetizations, average torques with segment n = 3 is higher than the torque with segment n = 4. The nonlinear flux leakages caused by n = 4 due to dual-rotor is the primary issue. In this paper, the segment n = 4 is selected for the following performance refinement since the torque ripple reduction is the priority for satellite applications. In next section, these leakage fluxes are reduced based on the rotor geometry design.

V. MOTOR GEOMETRIC DESIGN

After the design of dual-rotor, slots/poles combination and Halbach magnet, the motor geometry is finally adjusted to maximize the flux linkage while minimizing leakage fluxes. Table 4 lists key motor parameters and specification. It is noted that four parameters are selected for the geometric design. As shown in Fig. 11, they are the outer radius of outer

TABLE 3. Torque comparison among different Halbach array angles in Fig. 9.

Average torque [mNm]	Values
Radial magnetization	36.89
Halbach array n=2	37.40
Halbach array n=3	42.38
Halbach array n=4	38.79
Torque ripple [%]	**Values**
Radial magnetization	5.43
Halbach array n=2	3.91
Halbach array n=3	3.01
Halbach array n=4	1.34

TABLE 4. Parameters and specification of satellite motor.

Parameters	Values
Outer radius of outer rotor	R_{o_i}†
Inner radius of inner rotor	R_{i_i}†
Air gap radius	R_{g_i}†
Air gap length	g_i†
Rotor axial length	10 mm
Inner rotor magnet height	10 mm
Outer rotor magnet height	10 mm
Number of turns	48 turns
Rated power	11.5 W
Rated voltage	28 V
Phase resistance	0.794 Ω
Phase inductance	24.11 μH
Halbach magnet segment	4
Slot and pole numbers	9-slot-8-pole

†: Detail values cannot indicate because this motor will be used for the aerospace and defense application

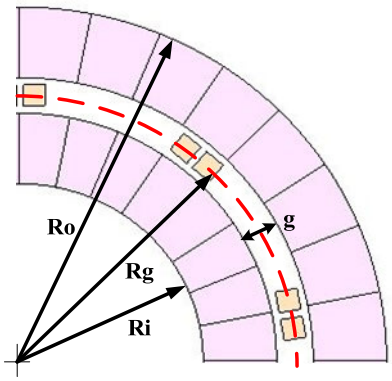

FIGURE 11. Key geometric parameters for the proposed satellite motor with dual-rotor and slotless stator.

rotor R_o, inner radius of inner rotor R_i, air gap radius R_g and air gap length g. The subscript i denotes the initial value.

In this section, these four parameters are determined based on the sensitivity analysis of flux linkage. On the basis, the flux linkage is analyzed with respect to single parameter change. The air gap radius is firstly adjusted to determine the relative positon between inner radius of inner rotor R_i, and outer radius of outer rotor R_o. After that, the air gap length g is analyzed to obtain the maximum available windings area.

A. AIR GAP RADIUS R_G DESIGN

The air gap radius R_g is firstly designed to maximize the magnet flux linkage. In this simulation, the flux linkage from both the inner rotor and outer rotor are separated analyzed.

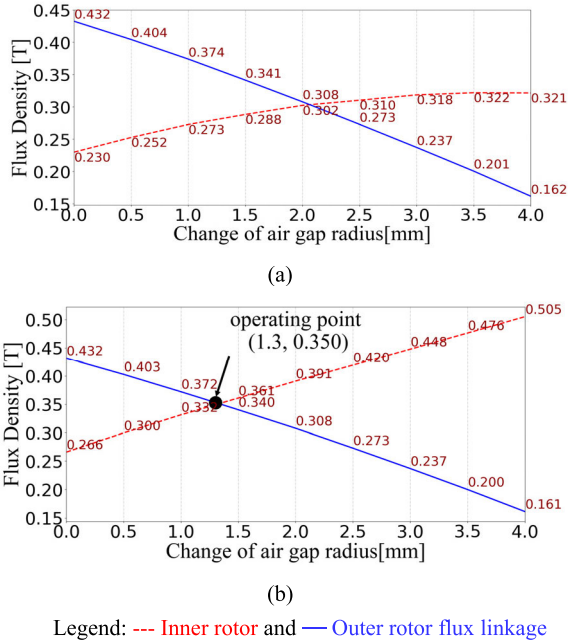

FIGURE 12. Flux density versus the change of air gap radius for both inner rotor and outer rotor: (a) Radial flux and (b) Tangential flux magnitude (9-slot-8-pole, Halbach magnets and no load).

For example, the outer rotor magnets are replaced by the stator iron core as a single-rotor motor for the analysis of inner rotor generated flux, as seen from the motor topology in Fig. 3(a). Similar process can be applied for the analysis of outer rotor flux from the topology in Fig. 3(b). Through finding peak flux magnitudes individually for inner and outer rotor, the highest flux linkage can be obtained on the proposed dual-rotor motor.

Fig. 12 shows the sensitivity analysis of (a) radial flux density B_{gr} and (b) tangential flux density $B_{g\theta}$ with respect to the change of R_g. In this analysis, different flux density waveforms versus the air gap radius R_g are calculated based on FEA. The corresponding peak flux density values are then compared under R_g change. For the sensitivity analysis, R_g is incrementally increased or decreased every 0.5mm from initial R_{g_i}. In addition, outer radius R_o and inner radius R_i are maintained same values for the geometric design. Both B_{gr} and $B_{g\theta}$ are obtained from the FEA simulation.

As seen for radial flux density B_{gr} versus R_g in Fig. 12(a), the inner rotor B_{gr} increases as R_g increases because of higher magnet volume in the inner rotor. By contrast, the outer rotor B_{gr} decreases as R_g increases due to lower magnet volume. Because the outer rotor has the bigger magnet volume than the inner rotor magnet, the total radial B_{gr} results in the highest flux density at initial R_{g_i}+0mm. However, it is important that the peak torque might not appear at R_{g_i}+0mm since the tangential $B_{g\theta}$ also affects the torque production.

Fig. 12(b) analyzes the tangential flux density $B_{g\theta}$ under the same change of R_g for either the inner or outer rotor. It is found that the inner rotor tangential $B_{g\theta}$ and outer rotor $B_{g\theta}$ are the same with 0.350T when R_g is designed

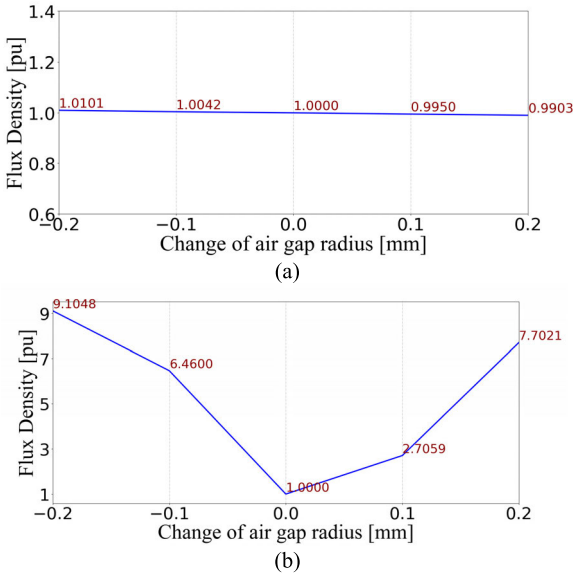

FIGURE 13. Flux density versus air gap radius for the proposed dual-rotor motor: (a) Radial flux and (b) Tangential flux magnitude (baseline air gap length is R_{g_i}+1.3mm).

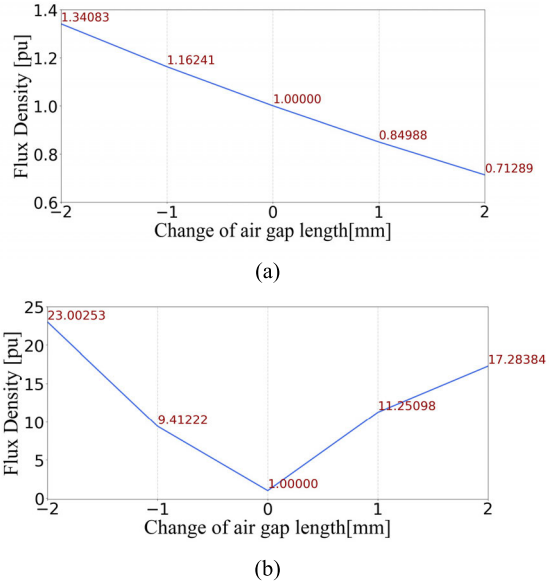

FIGURE 14. Flux density versus air gap length for the proposed dual-rotor motor: (a) Radial flux and (b) Tangential flux magnitude (baseline air gap length is R_{g_i}+1.3mm).

at R_{g_i}+1.3mm. This cross point results in the same tangential $B_{g\theta}$ of inner and outer rotor. Although the total radial B_{gr} at R_{g_i}+1.3mm is lower than B_{gr} at original R_{g_i}+0mm, it will be shown that the torque output is highest at R_{g_i} +1.3mm because the flux linkage is most concentrated once inner rotor $B_{g\theta}$ is equal to outer rotor $B_{g\theta}$.

After finding the optimal operating point where R_g = R_{g_i}+1.3mm, the flux density distribution of completed dual-rotor motor is then analyzed. Fig. 13 shows both (a) radial flux density B_{gr} and (b) tangential flux density $B_{g\theta}$ for the dual-rotor motor under the change of R_g. In this simulation, the flux density is represented by per unit value with respect to their initial values. Baseline values of B_{gr} and $B_{g\theta}$ are respectively 0.641T and 1.533mT.

As mentioned in section IV, the dual-rotor topology can concentrate the flux linkage because two rotors are individually used for the flux transmitter and receiver. Under this effect, $B_{g\theta}$ caused by leakage fluxes is minimized. Fig. 13(a) shows the radial flux density B_{gr} in the dual-rotor motor versus the change of designed air gap radius at R_{g_i}+1.3mm. The simulation condition is similar to Fig. 12 where peak values of flux density waveforms are compared under different geometries. It is observed that radial B_{gr} maintains at 1 p.u. under the change of R_g.

On the other hand, Fig. 13(b) shows the tangential flux density $B_{g\theta}$ versus R_g. As mentioned in Fig. 12(b), the optimal operating point R_{g_i}+1.3mm is designed at the same tangential $B_{g\theta}$ of inner and outer rotor. Under this effect, the flux linkage is most concentrated with the minimum leakage flux. Fig. 13(b) verifies this design approach. The tangential $B_{g\theta}$ significantly increases once R_g moves away from the operating point R_{g_i}+1.3mm. Therefore, the air gap radius is finally determined at R_{g_i} +1.3mm for the purpose of $B_{g\theta}$ minimization while B_{gr} is maintained.

B. AIR GAP LENGTH G DESIGN

This part aims to design the air gap length g. In general, the overall windings area can be increased by increasing g. It results in more armature fluxes for torque production. However, the increase of g decreases the flux linkage across slotless windings. Under this effect, it is worth to analyze the change of g on the flux linkage magnitude.

Fig. 14 shows (a) radial B_{gr} and (b) tangential $B_{g\theta}$ under the change of air gap length g in Fig. 11. In this simulation, the air gap radius is set at R_{g_i}+1.3mm based on the result at part A. Here, g is incrementally increased or decreased every 1mm. Per unit values similar to Fig. 13 are selected for the comparison.

As seen in Fig. 14(a), radial B_{gr} greatly decreases once air gap length g increases, leading to the torque reduction. However for the tangential density $B_{g\theta}$ in (b), a small change of g causes a considerable increase of leakage fluxes. Based on this simulation, the final air gap length g is determined at the initial vale g_i to minimize leakage fluxes in slotless windings.

C. PERFORMANCE COMPARISON

This part compares the flux density distribution for the dual-rotor motor after the geometric design. Fig. 15 compares (a) radial B_{gr} and (b) tangential $B_{g\theta}$ for the proposed motor before and after the design. As seen in Fig. 15(a), the radial B_{gr} magnitude maintains the same by changing the air gap radius to R_{g_i} +1.3mm. More importantly, the tangential $B_{g\theta}$ decreases 0.9565 times comparing to the baseline motor after the geometrical adjustment. In general, the torque output is

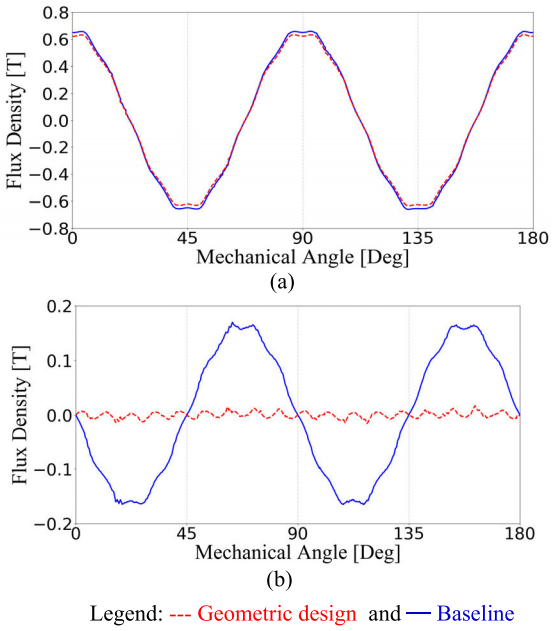

FIGURE 15. Comparison of (a) radial flux density and (b) tangential flux density for the dual-rotor slotless windings motor before and after the geometric design.

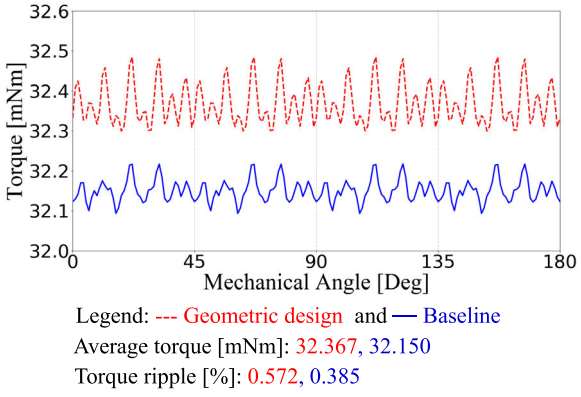

FIGURE 16. Comparison of torque output for the dual-rotor motor before and after the geometric design (9-slot-8-pole and Halbach magnets).

dependent on the interaction of B_{gr} and the armature current. However, the tangential $B_{g\theta}$ representing the leakage flux also affects the torque output. Under this effect, the higher electromagnetic torque is achieved by maximizing B_{gr} and minimizing low $B_{g\theta}$.

Fig. 16 compares the torque output for the proposed dual-rotor motor before and after the design. It is concluded that the average torque increases from 32.15mNm to 32.37mNm without adding additional windings and magnets.

D. AXIAL MAGNET LEAKAGE FLUX

Although magnet leakage fluxes along the rotor tangential direction are minimized through the geometric design, slotless windings also result in additional leakage fluxes across the axial direction. This part analyzes axial direction leakage fluxes based on 3-D FEA simulation.

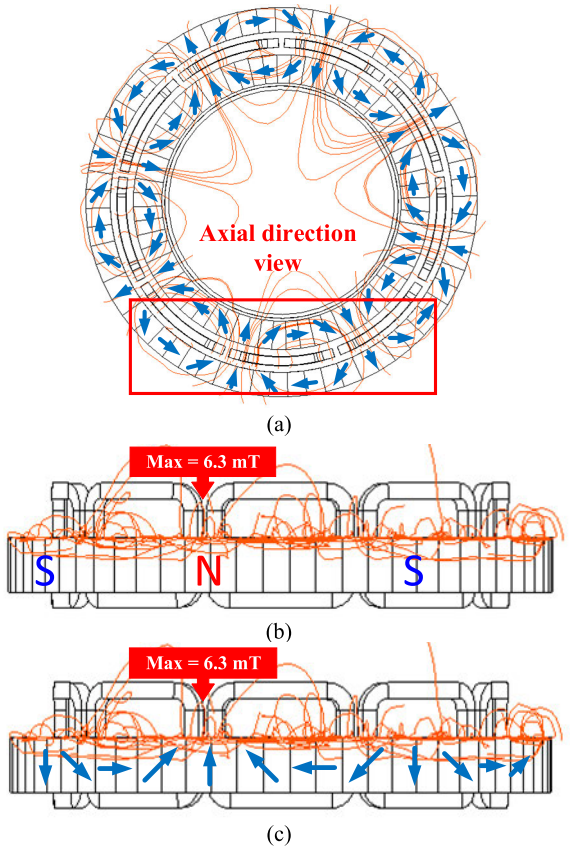

FIGURE 17. Illustration of magnet leakage fluxes across the axial direction for the slotless windings dual-rotor satellite motor: (a) axial direction view area, (b) axial flux distribution shown by magnet polarity and (c) axial flux distribution shown by Halbach magnet array (rated flux linkage 0.634T).

Fig. 17 shows the distribution of leakage fluxes along the axial direction. As seen in Fig. 17(b) and (c), the peak axial leakage flux occurs when the magnet magnetization direction is aligned with edge of two slotless windings. These axial leakage fluxes can be improved by decreasing the ending windings fluxes can be improved by decreasing the ending windings length. Nevertheless, axial leakage fluxes are around 1% with respect to the magnet flux linkage which can be negligible.

VI. EXPERIMENTAL TEST

This section illustrates the experimental verification of proposed satellite motor. Fig. 18 shows the proposed satellite motor prototype on the experimental test bench. A hysteresis dynamometer is connected to the motor for the load operation. In these experiments, the position sensorless field oriented control (FOC) is applied to drive the satellite motor. Pulse width modulation (PWM) frequency is set at 10kHz synchronizing with the sample frequency. The DC bus voltage is 24V to be compatible with the satellite electronics system. All the control and position sensing algorithms are implemented in a 32-bit microcontroller, TI-TMS320F28069.

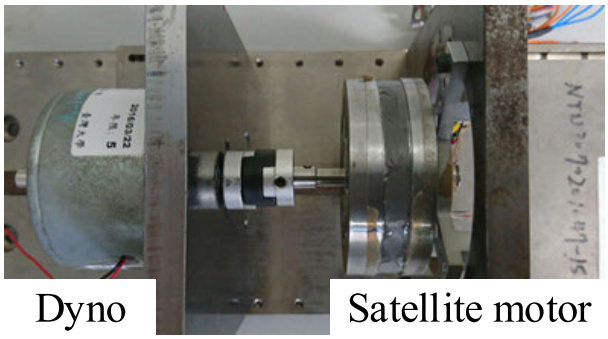

FIGURE 18. Illustration of designed satellite motor prototype and experimental test bench.

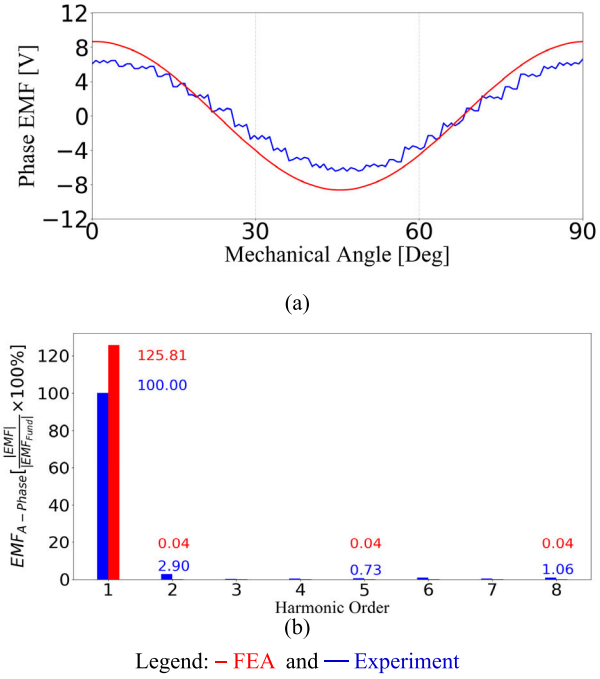

FIGURE 19. Illustration of (a) time-domain phase emf waveform and (b) the corresponding spectrum when the speed is at 6000rpm rated speed.

A. BACK EMF WAVEFORM

The back electromotive force (EMF) voltage waveform is firstly tested at this part. It is noted that the back EMF voltage is equivalent to the magnet flux times rotor speed. Because the flux density is not possible to obtain in actual experiments, the back EMF voltage is measured instead of magnet flux to evaluate the Halbach array magnet performance.

In this test, the PM motor is firstly accelerated to the rated speed of 6000rpm. After that, the electrical power is suddenly disable and the A-phase EMF voltage is measured based on the voltage probe. Fig. 19 shows the time-domain phase EMF waveform and the corresponding EMF spectrum respectively at 6000rpm. Instead of measured EMF waveform, the FEA simulation is compared to carefully evaluate secondary EMF harmonics and the motor manufacturing error. To easily compare different EMF spectrums, the per unit magnitude with respect to the fundamental harmonic of measured EMF is illustrated.

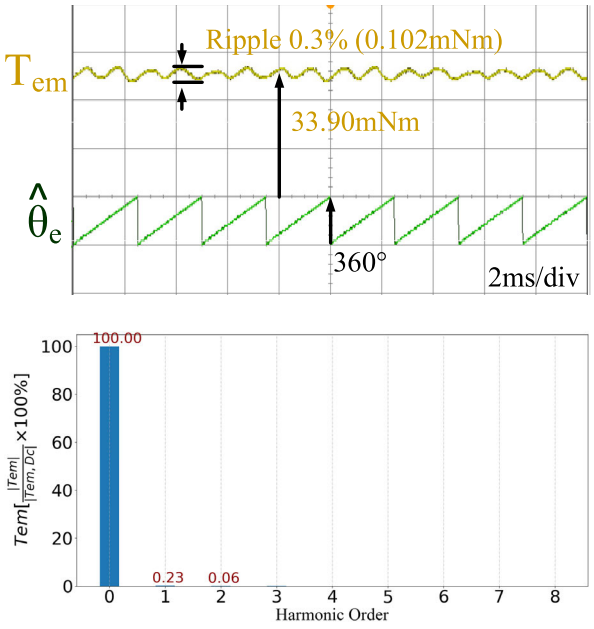

FIGURE 20. Time-domain torque waveform and corresponding harmonics (full load and 6000rpm speed).

It is shown that the measured EMF magnitude is 26% lower than the simulated EMF magnitude. For the actual prototype fabrication, different Halbach magnet segments are magnetized firstly and then glued together during the rotor assembly. It is observed that the axial leakage flux is increased in the actual prototype, leading to the EMF magnitude reduction. Besides comparing to FEA simulation waveform, 2nd-order and 8th-order EMF secondary harmonic occurs on the actual motor. These harmonics might be caused by the fabrication error during the magnet installation. Nevertheless, these two harmonic magnitudes are negligible comparing to the fundamental harmonic magnitude. It can be concluded that the Halbach array magnet proposed in section IV can achieve a nearly sinusoidal magnet flux for the smooth torque production.

B. ELECTROMAGNETIC TORQUE OUTPUT

At this part, the actual torque output and corresponding torque harmonics are evaluated. For the experimental setup, the rotor position $\hat{\theta}_e$ is estimated through the EMF-based position estimation. A constant q-axis current I_q in the rotor-referred synchronous frame is applied based on the current regulation with FOC. The electromagnetic torque T_{em} is then obtained by

$$T_{em} = K_t I_q \tag{6}$$

where K_t is the corresponding torque constant calculated by FEA. Fig. 20 shows the time-domain waveform of T_{em} and the corresponding torque harmonic spectrum. Here, $I_q = 1.314$A regulated by the current controller is applied.

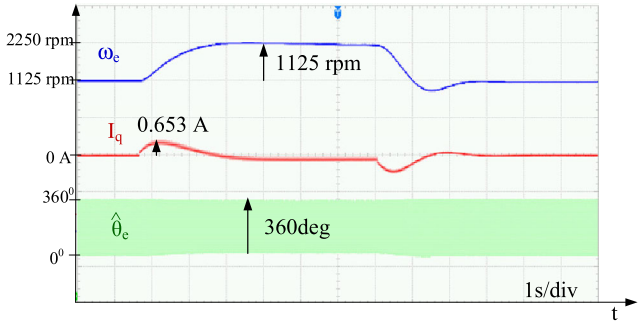

FIGURE 21. Time-domain waveforms of q-axis currents, rotor speed and rotor position under a trapezoidal speed command (speed changes from 1125rpm to 2500rpm).

The peak-to-peak torque ripple is around 0.3%. It is lower than the design specification, 1% in Table 1.

According to the torque spectrum in Fig. 20 the measured torque harmonics are primarily located at 1st-order with respect to the rotor frequency. It is noted that from Fig. 19, the 2nd-order EMF harmonic occurs on the phase EMF waveform. Considering the torque production, the interaction of fundamental EMF harmonic and phase current can generate the electromagnetic torque. Under this effect, the 2nd-order EMF harmonic should contribute to the 1st-order torque harmonic, as demonstrated in Fig. 20. It is also observed that the torque harmonic magnitude slightly increases due to additional misalignment on the rotor installation. Nevertheless, the torque harmonic magnitude is small comparing to the fundamental component. Based on this experiment, it is concluded that the proposed design of slotless windings, Halbach magnet and geometrical adjustment are all useful to generate the smooth torque output with low ripple.

C. SATELLITE ATTITUDE CONTROL MANIPULATION

This part manipulates the satellite attitude control using the proposed dual-rotor PM motor. Fig. 21 shows time-domain waveforms of q-axis currents I_q, rotor speed ω_e and estimated rotor position $\hat{\theta}_e$. In this experiment, the speed command is increased from 1125rpm to 2500rpm to simulate the attitude control illustrated in Fig. 2. It is found that the proposed satellite motor can accelerate to the desired speed within a certain amount of time. Under this effect, the satellite attitude can be maintained based on the angular momentum control, as mentioned in (5).

D. SENSORLESS BLDC vs. FOC

It is noted that FOC drive is implemented to evaluate the satellite motor performance at prior experimental tests. Although FOC can achieve the smooth torque production, additional current sensors might result in the reliability issue on aerospace applications. Under this effect, this part compares different position sensorless drives between the brushless DC (BLDC) control and FOC. In general, sensorless BLDC requires voltage sensors instead of current sensors.

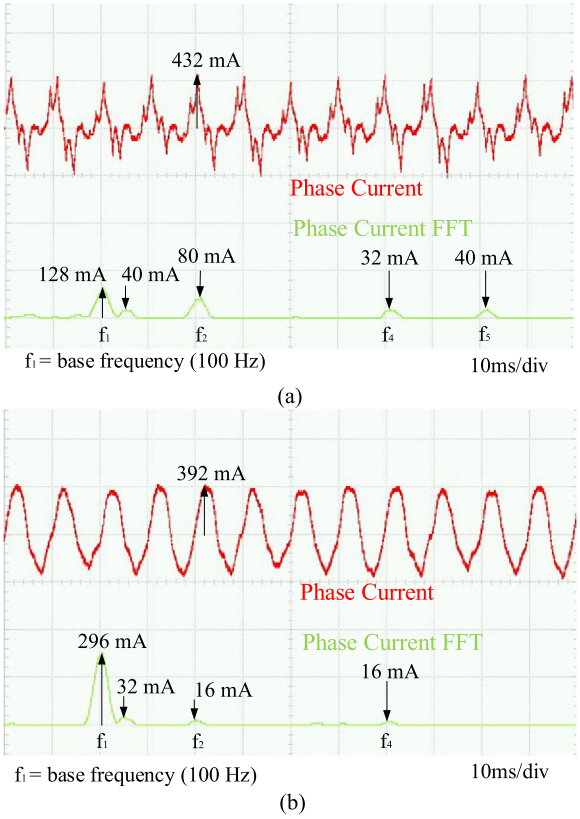

FIGURE 22. Phase current waveform comparison based on (a) BLDC drive and (b) FOC drive (rated torque and 1500 rpm).

Without using additional amplifiers or Hall-effect sensors, the drive reliability can be improved.

Fig. 22 compares different phase current waveforms and corresponding spectrums for the satellite motor drive using (a) BLDC and (b) FOC. In this test, the speed is controlled at 1500rpm under rated load. By comparing sensorless BLDC with FOC, additional current harmonics are resultant, increasing torque ripples and rotor losses. Nevertheless, sensorless BLDC can be used as a backup drive when sensor faults appear on the high-performance FOC drive.

VII. CONCLUSION

A slotless windings dual-rotor PM motor is proposed for the satellite attitude control. Slotless windings reflected leakage fluxes are minimized by designing two rotors respectively for flux transmitter and flux receiver. Besides, a nearly sinusoidal EMF voltage is realized by designing Halbach magnet array on this dual-rotor topology. All the proposed design methods are verified by FEA. A motor prototype is fabricated for the experimental evaluation and satellite attitude control.

REFERENCES

[1] M.-C. Chou, C.-M. Liaw, S.-B. Chien, F.-H. Shieh, J.-R. Tsai, and H.-C. Chang, "Development and control for a reaction wheel system driven by permanent magnet synchronous motor," in *Proc. 13th Int. Power Electron. Motion Control Conf.*, Sep. 2008, pp. 1652–1659, doi: 10.1109/EPEPEMC.2008.4635504.

[2] B. Xiao, M. Huo, X. Yang, and Y. Zhang, "Fault-tolerant attitude stabilization for satellites without rate sensor," *IEEE Trans. Ind. Electron.*, vol. 62, no. 11, pp. 7191–7202, Nov. 2015, doi: 10.1109/TIE.2015.2432107.

[3] J. G. Bitterly, "Flywheel technology past, present, and 21st Century projections," in *Proc. 32nd Intersociety Energy Convers. Eng. Conf. (IECEC)*, vol. 4, Jul./Aug. 1997, pp. 2312–2315, doi: 10.1109/IECEC.1997.658228.

[4] B. Xiao, S. Yin, and O. Kaynak, "Attitude stabilization control of flexible satellites with high accuracy: An estimator-based approach," *IEEE/ASME Trans. Mechatronics*, vol. 22, no. 1, pp. 349–358, Feb. 2017, doi: 10.1109/TMECH.2016.2614839.

[5] Z. Jibin, Y. Guodong, X. Yongxiang, C. Xia, L. Yong, and W. Qian, "Development of a slotless limited-angle torque motor for reaction wheels torque measurement system," *IEEE Trans. Magn.*, vol. 50, no. 11, pp. 1–4, Nov. 2014, doi: 10.1109/TMAG.2014.2320953.

[6] J.-E. Yi, K. W. Lee, B. Kim, J. Ko, S. Jeong, M. D. Noh, and S. S. Lee, "Micro flywheel energy storage system with axial flux machine," in *Proc. IEEE/ASME Int. Conf. Adv. Intell. Mechatronics*, Sep. 2007, pp. 1–6, doi: 10.1109/AIM.2007.4412409.

[7] Z. Ismail and R. Varatharajoo, "A study of reaction wheel configurations for a 3-axis satellite attitude control," *Adv. Space Res.*, vol. 45, no. 6, pp. 750–759, Mar. 2010.

[8] K. B. Ma, Y. Zhang, Y. Postrekhin, and W.-K. Chu, "HTS bearings for space applications: Reaction wheel with low power consumption for mini-satellites," *IEEE Trans. Appiled Supercond.*, vol. 13, no. 2, pp. 2275–2278, Jun. 2003, doi: 10.1109/TASC.2003.813064.

[9] O. Wallmark, P. Kjellqvist, and F. Meier, "Analysis of axial leakage in high-speed slotless PM motors for industrial hand tools," *IEEE Trans. Ind. Appl.*, vol. 45, no. 5, pp. 1815–1820, 2009, doi: 10.1109/TIA.2009.2027109.

[10] A. Looser, T. Baumgartner, J. W. Kolar, and C. Zwyssig, "Analysis and measurement of three-dimensional torque and forces for slotless permanent-magnet motors," *IEEE Trans. Ind. Appl.*, vol. 48, no. 4, pp. 1258–1266, Jul. 2012, doi: 10.1109/TIA.2012.2199070.

[11] N. Bianchi, S. Bolognani, and F. Luise, "Potentials and limits of high-speed PM motors," *IEEE Trans. Ind. Appl.*, vol. 40, no. 6, pp. 1570–1578, Nov. 2004, doi: 10.1109/TIA.2004.836173.

[12] S. Jumayev, K. O. Boynov, J. J. H. Paulides, E. A. Lomonova, and J. Pyrhonen, "Slotless PM machines with skewed winding shapes: 3-D electromagnetic semianalytical model," *IEEE Trans. Magn.*, vol. 52, no. 11, pp. 1–12, Nov. 2016, doi: 10.1109/TMAG.2016.2586740.

[13] J. Millinger, O. Wallmark, and J. Soulard, "High-frequency characterization of losses in fully assembled stators of slotless PM motors," *IEEE Trans. Ind. Appl.*, vol. 54, no. 3, pp. 2265–2275, May 2018, doi: 10.1109/TIA.2018.2806883.

[14] A. Tessarolo, M. Bortolozzi, and C. Bruzzese, "Explicit torque and back EMF expressions for slotless surface permanent magnet machines with different magnetization patterns," *IEEE Trans. Magn.*, vol. 52, no. 8, pp. 1–15, Aug. 2016, doi: 10.1109/TMAG.2016.2543682.

[15] D. Lee, A. Jin, B.-H. Min, L. Zheng, and K. Haran, "Optimisation method to maximise torque density of high-speed slotless permanent magnet synchronous machine in aerospace applications," *IET Electr. Power Appl.*, vol. 12, no. 8, pp. 1075–1081, Sep. 2018, doi: 10.1049/iet-epa.2017.0873.

[16] Z. Q. Zhu and D. Howe, "Halbach permanent magnet machines and applications: A review," *IEE Proc. Electr. Power Appl.*, vol. 148, no. 4, p. 299, 2001, doi: 10.1049/ip-epa:20010479.

[17] K. Liu, M. Yin, W. Hua, Z. Ma, M. Lin, and Y. Kong, "Design and analysis of Halbach ironless flywheel BLDC Motor/Generators," *IEEE Trans. Magn.*, vol. 54, no. 11, pp. 1–5, Nov. 2018, doi: 10.1109/TMAG.2018.2833958.

[18] L. Yang, J. Zhao, L. Yang, X. Liu, and L. Zhao, "Investigation of a stator-ironless brushless DC motor with non-ideal back-EMF," *IEEE Access*, vol. 7, pp. 28044–28054, 2019, doi: 10.1109/ACCESS.2019.2901632.

[19] L. Yang, J. Zhao, X. Liu, A. Haddad, J. Liang, and H. Hu, "Comparative study of three different radial flux ironless BLDC motors," *IEEE Access*, vol. 6, pp. 64970–64980, 2018, doi: 10.1109/ACCESS.2018.2878267.

[20] P. Liang, Y. Pei, F. Chai, Y. Bi, and S. Cheng, "An improved method for armature-reaction magnetic field calculation of interior permanent magnet motors," *IEEE Trans. Magn.*, vol. 52, no. 7, pp. 1–4, Jul. 2016, doi: 10.1109/TMAG.2016.2521873.

[21] T. Zhang, X. Ye, L. Mo, and Q. Lu, "Electromagnetic performance analysis on the bearingless permanent magnet synchronous motor with Halbach magnetized rotor," *IEEE Access*, vol. 7, pp. 121265–121274, 2019, doi: 10.1109/ACCESS.2019.2937897.

[22] F. Zhang, X. Ju, and H. Liu, "Electromagnetic design of 5MW dual-stator brushless doubly-fed generator with hybrid rotor," in *Proc. IEEE Transp. Electrific. Conf. Expo, Asia–Pacific (ITEC Asia–Pacific)*, Jun. 2016, pp. 832–836, doi: 10.1109/ITEC-AP.2016.7513064.

[23] F. Zhang, T. Tong, and H. Liu, "Design and analysis of 50KW dual-stator brushless doubly-fed generator for wind turbine," in *Proc. 20th Int. Conf. Electr. Mach. Syst. (ICEMS)*, Aug. 2017, pp. 1–5, doi: 10.1109/ICEMS.2017.8056427.

[24] Y.-H. Yeh, M.-F. Hsieh, and D. G. Dorrell, "Different arrangements for dual-rotor dual-output radial-flux motors," *IEEE Trans. Ind. Appl.*, vol. 48, no. 2, pp. 612–622, Mar. 2012, doi: 10.1109/TIA.2011.2180495.

[25] Y. Li, D. Bobba, and B. Sarlioglu, "Design and optimization of a novel dual-rotor hybrid PM machine for traction application," *IEEE Trans. Ind. Electron.*, vol. 65, no. 2, pp. 1762–1771, Feb. 2018, doi: 10.1109/TIE.2017.2739686.

[26] A. Darabi, H. Tahanian, S. Amani, and M. Sedghi, "An experimental comparison of disc-type hysteresis motors with slotless magnetic stator core," *IEEE Trans. Ind. Electron.*, vol. 64, no. 6, pp. 4642–4652, Jun. 2017, doi: 10.1109/TIE.2017.2674613.

[27] P.-H. Chou, S.-C. Yang, C.-J. Jhong, J.-I. Huang, and J.-Y. Chen, "High-precision permaent magent motor design for satellite attitude control with high torque density and low torque ripple," in *Proc. 45th Annu. Conf. IEEE Ind. Electron. Soc. (IECON)*, Oct. 2019, pp. 802–805, doi: 10.1109/IECON.2019.8926805.

[28] Z. Q. Zhu, M. L. M. Jamil, and L. J. Wu, "Influence of slot and pole number combinations on unbalanced magnetic force in PM machines with diametrically asymmetric windings," *IEEE Trans. Ind. Appl.*, vol. 49, no. 1, pp. 19–30, Jan. 2013, doi: 10.1109/TIA.2012.2229373.

PO-HUAN CHOU was born in Taipei, Taiwan, in 1982. He received the B.S. degree from Feng Chia University, Taiwan, in 2005, and the M.S. and Ph.D. degrees from National Dong Hwa University, Taiwan, in 2007 and 2011, respectively, all in electrical engineering. He is currently working with the Industrial Technology Research Institute. His research interests are in servo drive systems, intelligent control, DSP-based control systems, and motion control.

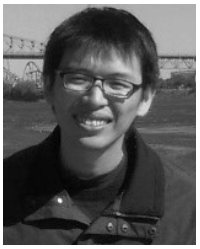

SHIH-CHIN YANG (Senior Member, IEEE) was born in Taiwan. He received the M.S. degree from National Taiwan University, Taiwan, in 2007, and the Ph.D. degree from the University of Wisconsin–Madison, WI, USA, in 2011, all in mechanical engineering. From 2011 to 2015, he was a Research Engineer with Texas Instruments Motor Laboratory, Dallas, TX, USA. He is currently an Associate Professor with National Taiwan University, with the responsibility on the development of motor drive and motor control technology. His research interests include motor drive, power electronics, and control systems. He was a recipient of the IEEE Industry Applications Society Industrial Drive Committee First Prize Paper Award, in 2011.

CIAO-JHEN JHONG received the B.S. degree in mechanical engineering from National Central University, Taoyuan, Taiwan, in 2018. She is currently pursuing the M.S. degree in mechanical engineering with National Taiwan University, Taipei, Taiwan. Her research interests include motor drive, control systems, and finite-element analysis of motor.

JEN-I HUANG was born in Taoyuan, Taiwan. He received the B.S. degree in mechanical engineering from National Central University, Taiwan, in 2018. He is currently pursuing the M.S. degree in mechanical engineering with National Taiwan University, Taiwan. His research interests include motor control systems, Hall-effect-sensor fault detection, and tolerant control.

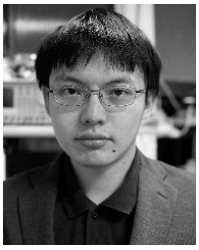

JYUN-YOU CHEN (Student Member, IEEE) was born in Taichung, Taiwan, in 1992. He received the B.S. degree in communication engineering from Feng Chia University, Taiwan, in 2015, and the M.S. degree in mechanical engineering from National Central University, Taiwan, in 2017. He is currently pursuing the Ph.D. degree and dissertation in mechanical engineering with National Taiwan University, Taiwan. His research interests are in motor drive and control systems.